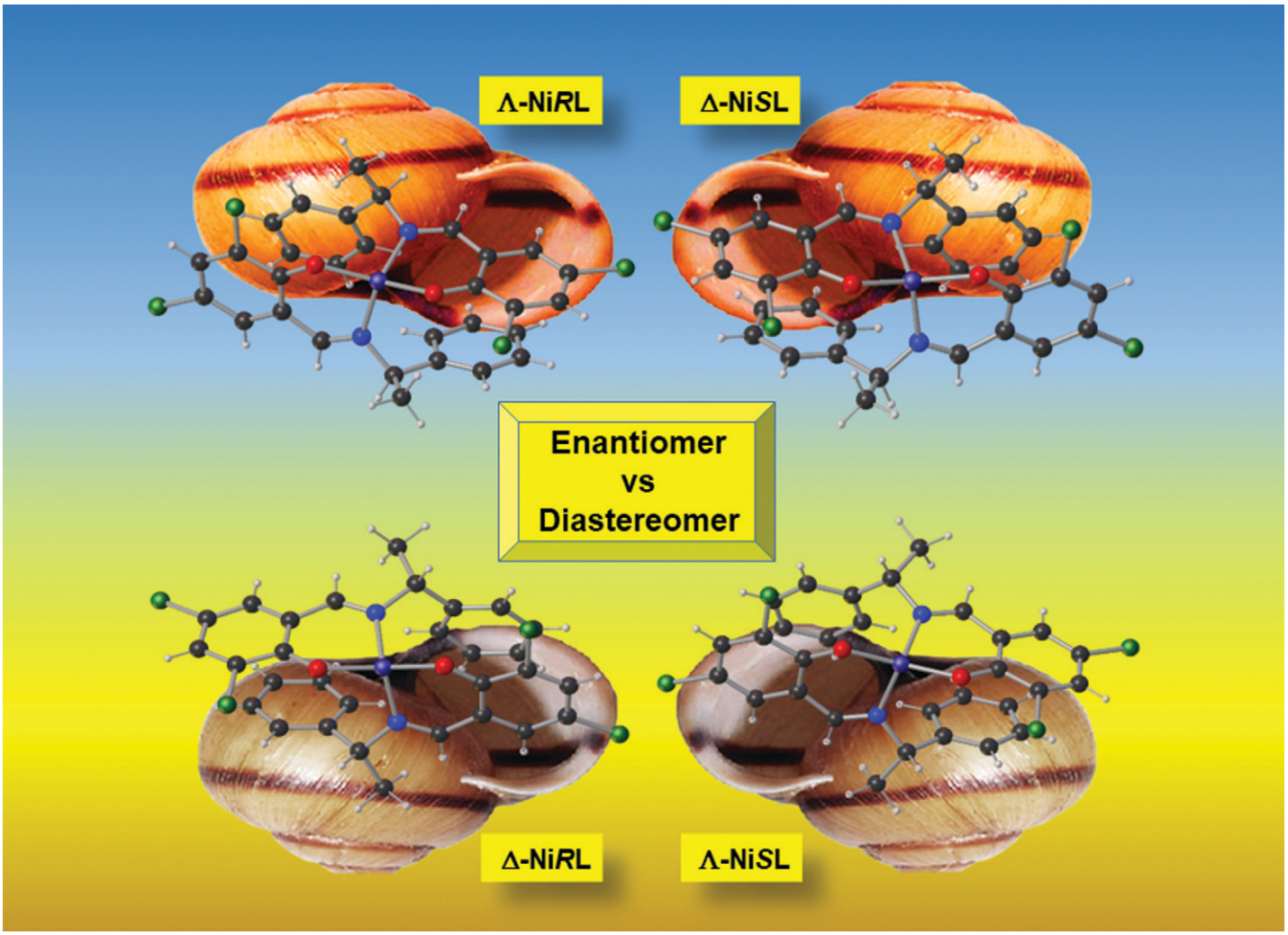

Showcasing research from Professor Mohammed Enamullah's laboratory, Department of Chemistry, Jahangirnagar University, Dhaka 1342, Bangladesh and Associate Professor Hadi Amiri Rudbari's laboratory, Department of Chemistry, University of Isfahan, Iran.

Experimental and computational studies on pseudotetrahedral nickel(II)-(*S*- or *R*-)-dihalogen-salicylaldiminates with Δ- or Λ-chirality induction at-metal

The manuscript describes synthesis and molecular structures of pseudotetrahedral C_2-symmetrical *bis*[(*S* or *R*)-N-1-(phenyl) ethyl-(2,4-dihalogen-salicylaldiminato-κ^2N,O)]-Δ/Λ-nickel(II), Δ/Λ-Ni(*S* or *R*)$L^{1\text{-}3}$ with Δ/Λ-chirality induction at-metal. The structural analysis features isolation of opposite configurred Δ-Ni or Λ-Ni diastereomer for *S*- or *R*-$HL^{1\text{-}3}$ ligands, resulting from diastereoselection and chirality induction at-metal. Electronic circular dichroism (ECD) spectra confirming enantiopurity/enantiomeric excess of Ni(*S* or *R*)$L^{1\text{-}3}$ in solution. Combined analyses of experimental and simulated ECD spectra suggest diastereomeric excess of Δ-Ni*S*$L^{1\text{-}3}$ or Λ-Ni*R*$L^{1\text{-}3}$ in solution, indicating preservation of chirality induction at-metal alike in solid state (or gas-phase optimized structures).

As featured in:

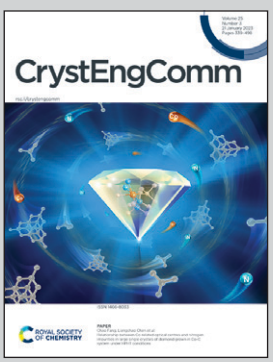

See Mohammed Enamullah *et al.*, *CrystEngComm*, 2023, **25**, 365.

ROYAL SOCIETY OF CHEMISTRY

rsc.li/crystengcomm

Registered charity number: 207890

CrystEngComm

PAPER

Cite this: *CrystEngComm*, 2023, **25**, 365

Experimental and computational studies on pseudotetrahedral nickel(II)-(*S* or *R*)-dihalogen-salicylaldiminates with Δ- or Λ-chirality induction at-metal†

Arezoo Saadati,[a] Hadi Amiri Rudbari, *[a] Mahnaz Aryaeifar,[a] Olivier Blacque,[b] Isabel Correia,[c] Mohammad Khairul Islam,[d] Dennis Woschko,[e] Takin Haj Hassani Sohi,[e] Christoph Janiak[e] and Mohammed Enamullah *[d]

In this study, three pairs of pseudotetrahedral C_2-symmetrical bis[(*S* or *R*)-*N*-1-(phenyl)ethyl-(2,4-X^1,X^2-salicylaldiminato-κ^2N,O)]-Δ/Λ-nickel(II), Δ/Λ-Ni*S*L^{1-3} or Λ/Δ-Ni*R*L^{1-3} (X^1, X^2 = Cl, Cl; Br, Br; Cl, Br) with Δ- or Λ-chirality induction at-metal were synthesized, respectively. X-ray molecular structures showed the formation of a N_2O_2-chromophore around nickel(II) from two molecules of Schiff bases in a pseudotetrahedral geometry. The structural analysis further suggested the isolation of opposite configured Δ-Ni and Λ-Ni diastereomers for *S*- and *R*-HL^{1-3} Schiff base ligands in an enantiopure crystal, resulting from diastereoselection and chirality induction at-metal. The gas-phase optimized structures for Δ-Ni*S*L^{1-3} or Λ-Ni*R*L^{1-3} are also slightly more stable by 0.10–1.70 kcal mol^{-1}. Electronic circular dichroism (ECD) spectra showed expected mirror-image relationships with opposite Cotton effects, confirming the enantiopurity or enantiomeric excess of Ni*R*L^{1-3} and Ni*S*L^{1-3} complexes in solutions. Combined analyses of experimental and simulated ECD spectra suggested diastereomeric excess of Δ-Ni*S*L^{1-3} or Λ-Ni*R*L^{1-3} in solutions, demonstrating the preservation of chirality induction at-metal alike in solid or gas phases. The analysis of supramolecular packing explored several kinds of intermolecular interactions with the strongest one for halogen···oxygen atoms and only halogen at the *para*-position of salicylaldehyde is involved in these interactions with Br···O > Cl···O. Hirshfeld surface analysis also supported such kind of interactions at a distance shorter than the sum of the van der Waals radii. The non-covalent interaction (NCI) indices explored the presence of weak attractive interactions resulting from the halogen atoms of the respective structures. The experimental and simulated PXRD patterns revealed a fair matching, confirming the phase purity of bulk crystal samples of these complexes.

Received 21st September 2022,
Accepted 7th November 2022

DOI: 10.1039/d2ce01311h

rsc.li/crystengcomm

Introduction

Four-coordinated non-planar transition metal(II)-complexes with asymmetric bidentate (A^B) ligands gained considerable interest in the context of syntheses, structural analyses, coordination geometry, chiroptical properties, (dia)stereoselectivity and induced Λ/Δ-chirality at-metal centres.[1–6] X-ray structural analyses revealed that the two molecules of A^B-chelate ligands coordinate to a metal ion forming a A_2B_2-chromophore with a pseudotetrahedral geometry. The formation of these molecules gives two opposite configured stereoisomers Λ-M(A^B) and Δ-M(A^B) with chirality induction at-metal in the C_2-symmetric molecules. In this connection, coordination of chiral asymmetric bidentate ligands (*R* or *S*-A^B) provides two opposite configured diastereomers Λ-M(*R*-A^B) and Δ-M(*R*-A^B) {or Δ-M(*S*-A^B) and Λ-M(*S*-A^B)} for each enantiopure ligand. However, the X-ray structure

[a] *Department of Chemistry, University of Isfahan, Isfahan 81746-73441, Iran*
[b] *Department of Chemistry, University of Zurich, Winterthurerstrasse 190, CH-8057, Zurich, Switzerland*
[c] *Centro de Química Estrutural, Institute of Molecular Sciences, Departamento de Engenharia Química, Instituto Superior Técnico, Universidade de Lisboa, Av. Rovisco Pais 1, 1049-001 Lisboa, Portugal*
[d] *Department of Chemistry, Jahangirnagar University, Dhaka 1342, Bangladesh. E-mail: enamullah@juniv.edu*
[e] *Institut für Anorganische Chemie und Strukturchemie, Heinrich-Heine Universität Düsseldorf, Universitätsstr. 1, D-40225 Düsseldorf, Germany*

† Electronic supplementary information (ESI) available: ESI contains the EI-mass spectra (Fig. S1); two-dimensional fingerprint plots and Hirshfeld surfaces (Fig. S2); relative contributions to the Hirshfeld surfaces (Fig S3); UV-vis spectra (Fig. S4 and S5); DFT optimized structures (Fig. S6); simulated UV-vis and ECD spectra (Fig. S7 and S8); opposite comparison of experimental and simulated ECD spectra (Fig. S9); ^{1}H NMR spectra (Fig. S10); excited state properties (Table S1). CCDC 2000643, 2000645, 2000647, 2000649, 2000651 and 2149672. For ESI and crystallographic data in CIF or other electronic format see DOI: **https://doi.org/10.1039/d2ce01311h**

determination indicates the formation and isolation of only one diastereomer of Λ-M(*R*-A^B) or Δ-M(*S*-A^B) in the bulk samples of enantiopure crystals in solid state.[7–15] Although the phenomenon is quantitative in the solid state (examined by X-ray structure and DSC analyses), both the diastereomers co-exist in solutions and lead to a diastereomeric equilibrium shift (*i.e.*, Λ ⇆ Δ) with temperature and/or time (examined by ^{1}H NMR, VCD and ECD spectra). The phenomenon is significantly influenced by ligand chirality and substituents, solute–solvent interactions in solutions, non-covalent interactions in solid, metal ion selection, crystallization protocols, solvent polarity, pH of the solution and redox reactions.[6–15]

Our recent studies on the diastereoselection phenomenon using the enantiopure Schiff base ligands {(*R* or *S*)-HL: L = (Ar)ethyl-salicylaldiminate[16a]/-naphthaldiminate[16b]} provide, in general, only one diastereomer of Λ-M*R*L or Δ-M*S*L (M = Co,[7,10] Ni,[13,15] Cu,[8] Zn[6a,9]) in a single enantiopure crystal, while in a single case opposite configured Δ-Cu*R*L or Λ-Cu*S*L is reported in Cu(II)-salicylaldiminate.[6b] However, in two cases both the diastereomers Λ- and Δ-M(*R* or *S*)L co-exist in a single enantiopure crystal.[2c,8] Due to various inter- and/or intra-molecular interactions, the only diastereomer Λ-M*R*L or Δ-M*S*L found in the solid state might not necessarily be the same as thermodynamically favored diastereomers formed in solution or gas phase (optimized structure). Thus, solid *versus* solution studies demonstrated preservation[6a,7–11,13,14] or inversion[6b,12] of chirality induction at-metal, suggesting a phase-dependent diastereoselection phenomenon. Combined analyses of experimental and simulated ECD spectra suggest, in general, the preservation of chirality leading to diastereomeric excess of Λ-M*R*L or Δ-M*S*L in solutions, in parallel to the diastereomers found in the solid state or gas phase (optimized structures). However, the introduction of dihalogen substituents in the chelate ring (salicylal-ring) results in chirality inversion from Λ-Cu*R*L$^{1-3}$ or Δ-Cu*S*L$^{1-3}$ in the solid state to Δ-Cu*R*L$^{1-3}$ or Λ-Cu*S*L$^{1-3}$ in solution or gas phase in Cu(*R* or *S*)L$^{1-3}$ complexes {L$^{1-3}$ = (phenyl)ethyl-2,4-X^1,X^2-salicylaldiminate and X^1, X^2 = Cl, Cl; Br, Br; Cl, Br}.[12] Conversely, the analogous homoleptic Λ- or Δ-Zn(*R* or *S*)L$^{1-3}$ complexes[14] show chirality preservation in the solid state and in solution (or gas phase optimized structures). In addition, variable time and temperature ^{1}H NMR spectra (along with simulation) showed the formation of only one diastereomer for the later Zn complexes (*i.e.*, Λ-Zn*R*L$^{1-3}$ or Δ-Zn*S*L$^{1-3}$)[14] instead of showing both diastereomers of Λ- and Δ-Zn(*R* or *S*)L {L = (Ar)ethyl-salicylaldiminate[6b]/-naphthaldiminate[9]} with an uneven ratio in solutions. These discrepancies in diastereoselection and chirality induction at-metal for a particular ligand with Cu[12] or Zn[14] lead to the present investigation on the homoleptic Ni(*R* or *S*)L$^{1-3}$ complexes. The single-crystal X-ray diffractions were carried out to elucidate the absolute configuration of the metal centre. Experimental and computational procedures on UV-vis and ECD spectra were employed to get insights into chiroptical properties and to assess the Λ- or Δ-chirality induction at-metal in solutions. Experimental and simulated powder XRD patterns were compared to check the phase purity of the bulk crystal samples of the complexes. The supramolecular packing analysis was conducted and linked with the Hirshfeld surfaces using CrystalExplorer.

Results and discussion

The reaction of enantiopure Schiff bases (*S* or *R*)-*N*-1-(phenyl) ethyl-2,4-X^1,X^2-salicylaldimine {(*S* or *R*)-HL$^{1-3}$: X^1, X^2 = Cl, Cl; Br, Br; Cl, Br} with $Ni(NO_3)_2{\cdot}6H_2O$ in the presence of triethylamine under reflux provides pseudotetrahedral C_2-symmetrical bis[(*S* or *R*)-*N*-1-(phenyl)ethyl-(2,4-X^1,X^2-salicylaldiminato-κ^{2}N,O)]-Δ/Λ-nickel(II), Δ/Λ-Ni*S*L$^{1-3}$ or Λ/Δ-Ni*R*L$^{1-3}$, respectively (Scheme 1). The elemental analysis data correspond well to the proposed compositions of the complexes, as depicted in the reaction in Scheme 1. IR spectra show the main characteristic band at *ca.* 1600 cm^{-1} for ν(C═N). EI-mass spectra display the parent ion peaks at 644 for Ni(*R* or *S*)L^1 ([M$^+$]), 823 for Ni(*R* or *S*)L^2 ([M + H$^+$]) and 734 for Ni(*R* or *S*)L^3 ([M$^+$]) (Fig. S1†). The spectra further reveal several ion peaks at 351, 441 and 397 for the mono-ligated species and at 292 for [HL^1–H]$^+$, 383 for [HL^2]$^+$ and 338 for [HL^3]$^+$, respectively.

Analyses of X-ray molecular structures

Solid-state X-ray molecular structures for the enantiopure crystals of bis[(*S* or *R*)-*N*-1-(phenyl)ethyl-(2,4-X^1,X^2-salicylaldiminato-κ^{2}N,O)]-Δ/Λ-nickel(II), Δ/Λ-Ni*S*L$^{1-3}$ or Λ/Δ-Ni*R*L$^{1-3}$ are shown in Fig. 1, and the selected bond lengths and angles are given in Table 1. All the complexes crystallize in non-centrosymmetric space groups (monoclinic, *I*2). The asymmetric unit contains half of the molecule that lies on a crystallographic 2-fold axis passing through the nickel center. The molecular structure features the nickel(II) ion surrounded by a N_2O_2-chromophore comprising two phenolate-oxygen and two imine-nitrogen atoms from two molecules of the Schiff bases in a pseudotetrahedral geometry. The inspection of metal–ligand bond distances reveals that the metal–oxygen bond is slightly shorter than the metal–nitrogen bond and indicates strong bonding between the negatively charged oxygen atom and the metal ion (Table 1). The N1–Ni–N1′ and O1–Ni–O1′ angle values are exactly the same for each enantiomeric pair, resulting in a fair overlap between them (*i.e.*, all atoms' sites overlap well). For example, an overlay plot of Λ-Ni*R*L^2 and Δ-Ni*S*L^2 is shown in Fig. 2 with the resulting r.

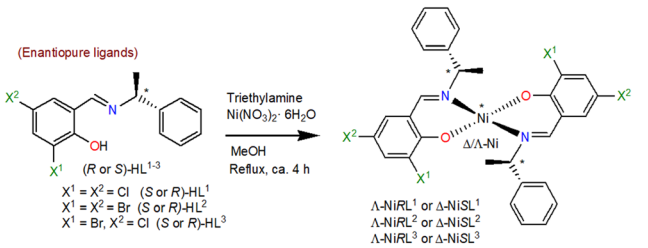

Scheme 1 Synthetic route for the formation of Δ/Λ-Ni(II)-(*S* or *R*)-Schiff base complexes.

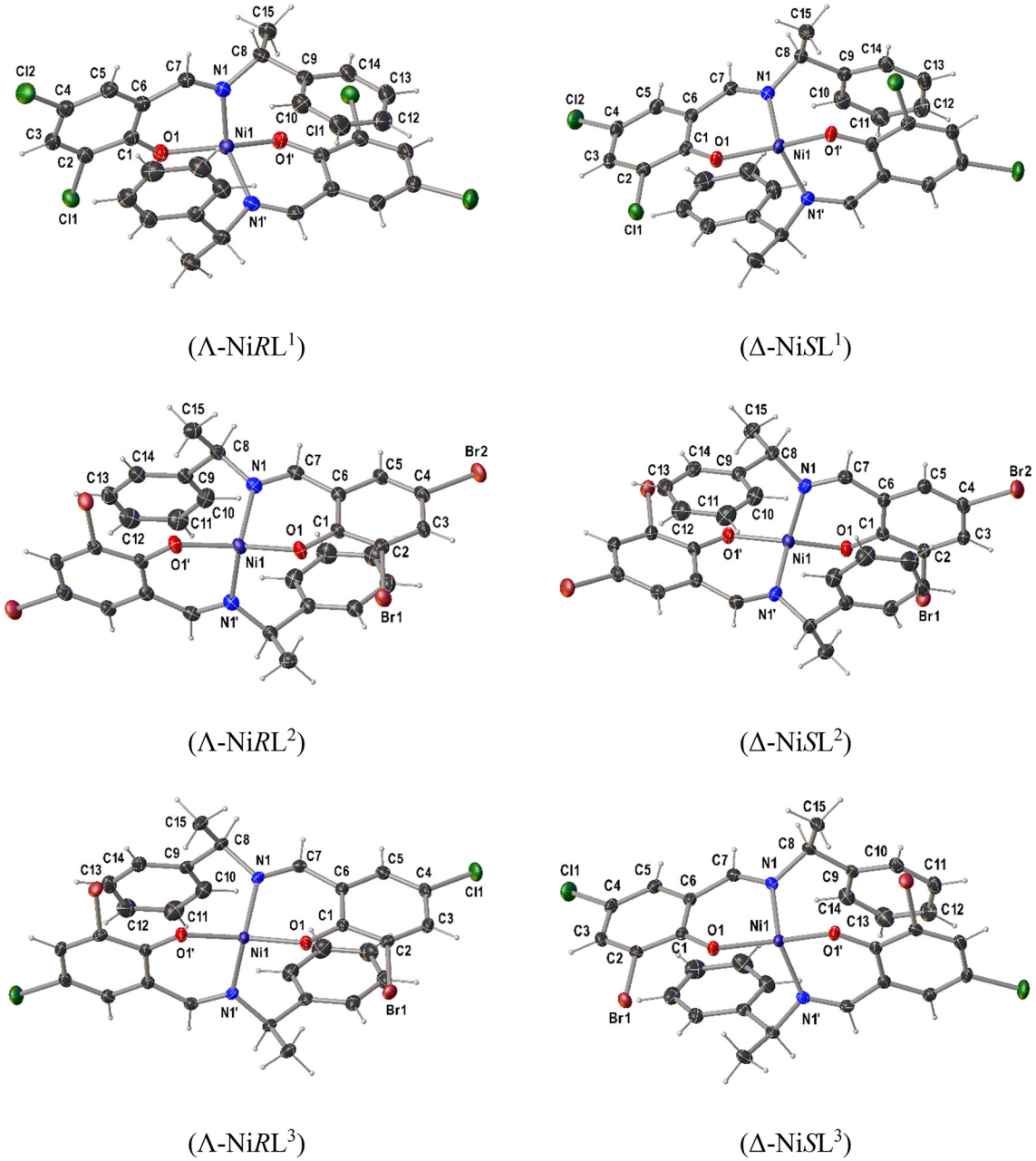

Fig. 1 Molecular structures for nickel(II)-Schiff base complexes with Λ-Ni*R*L$^{1-3}$ or Δ-Ni*S*L$^{1-3}$ configurations at-metal in the pseudotetrahedral geometry. Thermal ellipsoids are drawn at the 30% probability level, while the hydrogen size is arbitrary (see Table 1 for bond lengths and angle values).

Table 1 Selected bond lengths (Å) and angles (°) in Ni(II)-Schiff base complexes (Λ-Ni*R*L$^{1-3}$ and Δ-Ni*S*L$^{1-3}$)

	Λ-Ni*R*1	Λ-Ni*R*2	Λ-Ni*R*3	Δ-Ni*S*1	Δ-Ni*S*2	Δ-Ni*S*3
Ni1–O1/O1′	1.9103(17)	1.900(4)	1.9120(16)	1.910(2)	1.906(2)	1.9098(17)
Ni1–N1/N1′	2.008(2)	2.015(5)	2.0066(19)	1.998(3)	2.012(3)	2.006(2)
C7–N1	1.284(3)	1.274(8)	1.285(3)	1.293(4)	1.281(4)	1.285(3)
O1–Ni1–O1′	142.33(11)	142.9(3)	141.94(10)	142.37(14)	142.60(15)	142.50(11)
N1–Ni1–N1′	115.84(12)	115.3(3)	117.02(11)	115.92(15)	115.24(16)	116.61(12)
O1–Ni1–N1′	107.26(8)	107.12(19)	107.29(7)	107.24(10)	107.33(11)	107.04(8)
O1–Ni1–N1	92.65(8)	92.62(19)	92.49(7)	92.62(10)	92.61(10)	92.56(7)

Symmetry transformations used to generate equivalent atoms: 1 − *X*, + *Y*, 1 − *Z*.

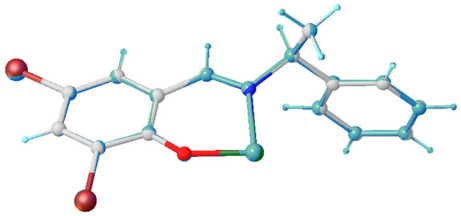

Fig. 2 Structural overlay plot of Λ-Ni*R*L^2 (blue) and Δ-Ni*S*L^2 (grey).

m.s. distance of 0.27 Å. The values of dihedral angles (θ = 74.3–75.5°) and geometric indexes ($\tau_{tet\text{-}sq}$ = 0.83–0.84), calculated from the X-ray structures, are listed in Table 2, are almost the same for all Ni(II)-complexes irrespective of different substituents on the salicylal-ring and in good accordance with the homoleptic Cu (θ = 60.1–62.0°)[12] or Zn (θ = 75.4–76.1°)[14] complexes. These values are very close to the corresponding values from DFT optimized structures (Table 2). These geometric parameters suggest a deviation from tetrahedral to pseudotetrahedral geometry by *ca.* 15° for Ni- or Zn-complexes, while from tetrahedral to distorted square-planar geometry by *ca.* 30° for Cu-complexes.[7–14,17] A stronger deviation for the Cu-complexes from tetrahedral, that is, a closer metal configuration to square-planar for Cu makes the Cu(chelate)$_2$ complexes more likely for chirality inversion if the solid and solution state have opposite ground-state energies for the Λ or Δ configuration (discussed below).

Considering the C_2-axis passing through the center of the O1···O1′ edge, metal ion and center of the N1···N1′ edge, the absolute configuration of the metal center was determined on the basis of very low absolute structure or Flack parameter values (−0.024 to −0.004).[18,19] Thus, for a given *S*- or *R*-ligand chirality, the Δ-Ni*S*L$^{1-3}$ or Λ-Ni*R*L$^{1-3}$ diastereomer was found in a single enantiopure crystal.[6–14] The Δ- or Λ-configuration at-metal is induced diastereospecifically by conformational preference of the chiral N,O-chelate rings and/or minimum steric requirements by ligand substituents in the coordination sphere, leading to thermodynamically stable Δ-Ni*S*L$^{1-3}$ or Λ-Ni*R*L$^{1-3}$ diastereomers. These results are in parallel to the preferred, in general, formation of Λ-M*R*L or Δ-M*S*L diastereomers in C_2-symmetrical metal-(*R* or *S*)-(Ar)-salicylaldiminate/naphthaldiminate complexes (metal = Co,[7,10] Ni,[13,15] Cu,[8] Zn[6a,9]) in the pseudotetrahedral geometry. Indeed, the homoleptic M(II)-(*S* or *R*)-*N*-1-(phenyl) ethyl-2,4-X^1,X^2-salicylaldiminates showed similar results of Δ- or Λ-chirality induction at-metal and provided the Δ-M*S*L$^{1-3}$ or Λ-M*R*L$^{1-3}$ configured diastereomer (M = Cu,[12] Zn[14]) in the solid state. However, it should be noted that the measurement of a single crystal in a single attempt does not exclude the presence of opposite configured diastereomers (*i.e.*, Λ-M*S*L$^{1-3}$ or Δ-M*R*L$^{1-3}$, may be minor) in the bulk crystal sample of the complexes.

Table 2 Values of dihedral angle (θ/°) and geometric index ($\tau_{tet\text{-}sq}$) in Ni(II)-Schiff base complexes (Λ-Ni*R*L$^{1-3}$ and Δ-Ni*S*L$^{1-3}$)[a]

Complexes	X_1, X_2	θ/°	$\tau_{tet\text{-}sq}$[b]
Λ-Ni*R*L^1	Cl, Cl	75.09 (71.00)	0.83 (0.79)
Δ-Ni*S*L^1	Cl, Cl	75.02 (71.00)	0.83 (0.79)
Λ-Ni*R*L^2	Br, Br	75.24 (65.60)	0.84 (0.73)
Δ-Ni*S*L^2	Br, Br	75.49 (65.51)	0.84 (0.73)
Λ-Ni*R*L^3	Cl, Br	74.34 (66.00)	0.83 (0.73)
Δ-Ni*S*L^3	Cl, Br	74.33 (66.29)	0.83 (0.74)

[a] Values in parentheses are from optimized structures. [b] $\tau_{tet\text{-}sq} = \theta/90$.

Supramolecular packing analyses

All the Ni(II)-Schiff base complexes show a similar crystal packing and feature several kinds of intermolecular interactions such as X···H–C, X···O, X···π, X···M, H···C, H···O and H···H, respectively. Because of the presence of the halogen atoms as substituents on the salicylal-ring (chelate-ring), most of the strong intermolecular interactions belong to these halogen atoms with other atoms. Among these interactions, the strongest one is identified as halogen···oxygen (X···O). It should be noted that only the halogens in the *para* position can involve in X···O interaction. According to X···O interaction values in Table 3, Br···O(1) interaction is the strongest one compared to Cl···O(1). The van der Waals (vdW) radii for the Cl, Br and O atoms are 1.76, 1.87, and 1.58 Å, respectively, and the corresponding sum of the vdW radii are Cl + O = 3.34 and Br + O = 3.45 Å.[20] As a result, X···O halogen bonding interactions play a key role in crystal packing with the Br atom in the *para* position of salicylaldehyde, as shown for Λ-Ni*R*L^2 in Fig. 3. Another strong intermolecular interaction in crystal packing is X···π contact. The geometrical parameters for C–Cl···π/C–Br···π interactions are listed in Table 4. The *ortho* halogen atom has an X···π interaction with the neighboring molecules and *vice versa*. According to geometric parameters in Table 4, especially the r_b value which is slightly shorter than the sum of the vdW radii for the halogen and carbon atoms (*i.e.*, $r_C + r_{Cl}$ = 3.45 Å and $r_C + r_{Br}$ = 3.55 Å), these interactions can be categorized as strong localized (SL) interactions.[12]

The supramolecular packing is further supported by analyses of intermolecular interactions with Hirshfeld surfaces using the program CrystalExplorer.[21,22] Because of similar Hirshfeld surfaces for all complexes, the Hirshfeld surface with d_{norm} properties and fingerprint plot only for Λ-Ni*R*2 are illustrated in Fig. 4 (for other complexes, see Fig. S2†). The percentages of contributions to various types of contacts in the fingerprint plots are summarized in Fig. S3.† The plots indicate that the highest contributions over the Hirshfeld surfaces are due to the H-atom with other atoms such as carbon (H···C), halogen (H···X) and hydrogen (H···H) (Fig. S3†). These three kinds of contacts overall are more than 84% of the total Hirshfeld surface area of the complexes. Also, the fingerprint plots indicate that the intermolecular interactions between the halogen and other atoms (X···X/C/H/O/M) cover nearly 40% of the whole Hirshfeld surfaces (Fig. S3†). This can be attributed to the relatively large vdW radii of the halogen atoms. The Hirshfeld surface analyses display strong

Table 3 Values of X···O(1) interactions in nickel(II)-Schiff bases complexes

Complexes	X =	X···O(1)/Å	C(4)–X···O(1)/°	C(1)–O(1)···X/°	<or> normal X···O bond (%)
Λ-Ni*R*L^1	Cl(2)	3.3526(18)	143.503	145.087	+0.38
Δ-Ni*S*L^1	Cl(2)	3.356(2)	143.463	144.958	+0.47
Λ-Ni*R*L^2	Br(2)	3.311(4)	142.747	143.963	−4.02
Δ-Ni*S*L^2	Br(2)	3.313(2)	143.026	144.058	−3.97
Λ-Ni*R*L^3	Cl(1)	3.3806(17)	143.299	144.688	+1.22
Δ-Ni*S*L^3	Cl(1)	3.3721(18)	143.387	144.842	+0.96

intermolecular interactions, between two molecules at a distance shorter than the sum of the vdW radii, as red spot on the d_{norm} surface in Fig. 4 (Fig. S2†). These strong intermolecular interactions include X···H/C/O and C···H contacts, respectively, which cover nearly 61% of the whole Hirshfeld surfaces (Fig. S3†). As we see in Fig. S3,† halogen atoms exist in three of four kinds of these strong interactions, indicating its prominent role in crystal packing.

The non-covalent interactions (NCI) are further investigated *via* NCIPLOT4 analysis.[33] Analysis is focused merely on the halogen bonds. Considering the peaks present in the NCI plots in Fig. 5 of Δ-Ni*S*L^1, Δ-Ni*S*L^2 and Λ-Ni*R*L^3 at *ca.* $-0.01 \leq \mathrm{sign}(\lambda_2)\rho \leq 0$ (λ_2: second eigenvalue of the Hessian of ρ), which represent weak attractive interactions in van der Waals regions, one can identify intermolecular Cl2···Cl1 and Cl2···O1 interactions between molecules of Δ-Ni*S*L^1, Br2···Br1 and Br2···O1 interactions between dimers of Δ-Ni*S*L^2, and Cl1···Br1 and Cl1···O1 interactions between molecules of Λ-Ni*R*L^3, among other interactions displayed in Fig. 5. The NCIPLOT indices therefore give further evidence to the presence of weak attractive interactions resulting from the halogen atoms of the respective structures.

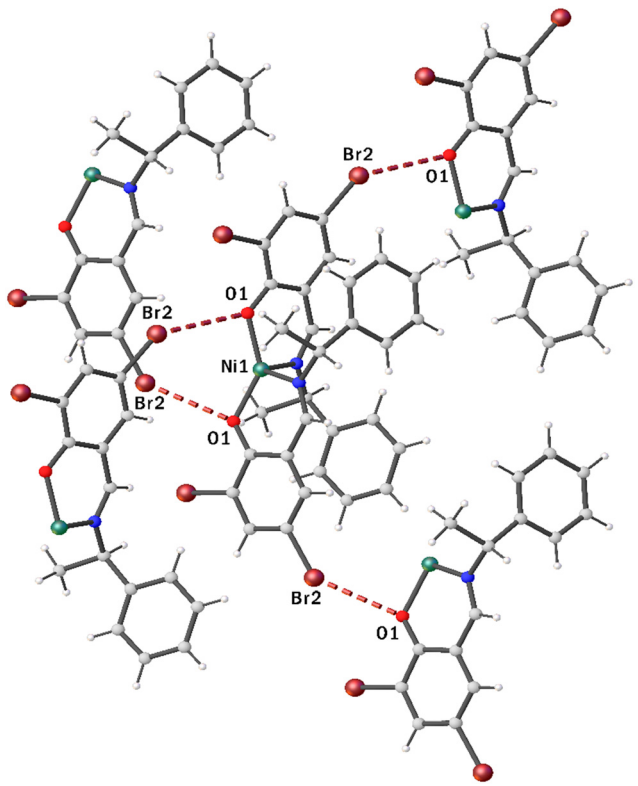

Fig. 3 Br···O(1) halogen bonding interactions in crystal packing of Λ-Ni*R*L^2.

Experimental UV-vis and ECD spectra

The absorption spectra (UV-vis) for the Schiff bases and nickel(II)-Schiff base complexes in methanol/chloroform (50%, v/v) (Fig. 6 and S4 and S5†) show several bands/shoulders at <500 nm, assigned to the intra-ligand (LL) and metal–ligand (ML) charge transfer transitions. The spectra for the complexes further reveal an additional weak broad band in the visible region due to the metal-centred d–d (MM) transitions for the nickel(II)-core electrons (Fig. 5 and S5;† inset).[13,15] The electronic circular dichroism (ECD) spectra for the complexes in methanol/chloroform (50%, v/v) (Fig. 7) display several bands with expected mirror image relationships, corresponding to the enantiopurity or enantiomeric excess of Ni*R*L$^{1-3}$ or Ni*S*L$^{1-3}$ in solutions.[8–14] The inspection of ECD spectra shows the following series of bands with opposite Cotton effects (sign and strength) at *ca.* 650 nm (−/+ and weak), 550 nm (+/− and weak), 495 nm (−/+ and very weak), 390 nm (+/− and strong), 330 nm (−/+ and weak), 280 nm (+/− and very strong) and 250 nm (−/+ and strong), respectively for Ni*R*L$^{1-3}$/Ni*S*L$^{1-3}$.

Optimized structures and excited state properties (Λ *vs.* Δ configuration at-metal)

Gas-phase optimized structures (Fig. S6†) for the diastereomeric pairs of Λ-Zn*R*L$^{1-3}$/Δ-Zn*R*L$^{1-3}$ and Λ-Zn*S*L$^{1-3}$/Δ-Zn*S*L$^{1-3}$ at b3lyp/6-31G(d) suggest diastereomeric preference with a very small amount of energy for Λ-Ni*R*L$^{1-2}$ or Δ-Ni*S*L$^{1-2}$ by 0.10–1.70 kcal mol^{-1}, alike the homoleptic Cu^{12}/Zn^{14} complexes. The excited state properties by TD-DFT were calculated at the same level of theory for Λ-Zn*R*L$^{1-2}$/Δ-Zn*R*L$^{1-2}$ and Λ-Zn*S*L$^{1-2}$/Δ-Zn*S*L$^{1-2}$ diastereomers, respectively. The simulated UV-vis spectra for all diastereomers are essentially identical (Fig. S7†), while ECD spectra show expected mirror-image relationships for each diastereomeric pair, respectively (Fig. S8†). Further, the simulated UV-vis spectra are almost identical to the experimental spectra in solution with a slight shifting of the band maxima (Fig. 6).

Comparison of experimental and simulated ECD spectra has been successfully used to assign the absolute

Table 4 Geometrical parameters (Å and °) for descriptions of C–X···π interactions in nickel(II) complexes

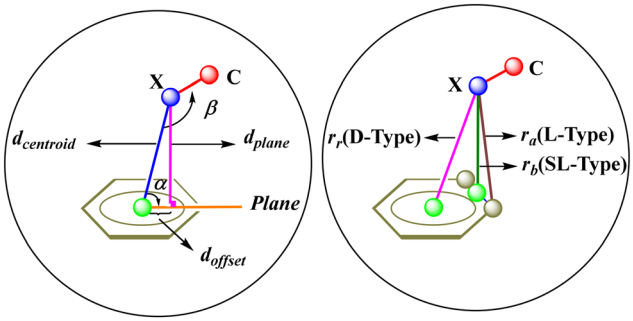

Definition of geometrical C–X···π parameters

	Λ-Ni*RL*^{1}/Δ-Ni*SL*^{1}	Λ-Ni-*RL*^{2}/Δ-Ni*SL*^{2}	Λ-Ni*RL*^{3}/Δ-Ni*SL*^{3}
C–X···π^a	C–Cl$_1$···π	C–Br$_1$···π	C–Br$_1$···π
r_r/Å	3.828/3.819	3.748/3.754	3.734/3.729
r_a/Å	3.528/3.518	3.467/3.474	3.430/3.430
r_b/Å	3.46/3.45	3.40/3.40	3.36/3.36
D_{plane}/Å	3.422/3.413	3.348/3.354	3.339/3.341
$d_{centroid}$/Å	3.828/3.819	3.748/3.754	3.734/3.729
d_{offset}/Å	1.715/1.713	1.687/1.686	1.670/1.657
α/°	63.38/63.34	63.28/63.30	63.43/63.62
β/°	144.11/144.13	144.97/144.88	145.26/145.23
Type	SL	SL	SL

^{a} π (C$_9$–C$_{14}$).

configuration of the metal centre in the complexes, resulting from diastereoselection and Λ- or Δ-chirality at-metal induced by the *R*- or *S*-ligands upon coordination.[6–14] The results show a fair matching of experimental spectra for Ni*RL*$^{1-2}$ or Ni*SL*$^{1-2}$ with simulated spectra for Λ-Ni*RL*$^{1-2}$ or Δ-Ni*SL*$^{1-2}$ diastereomer with a slight blue shifting of the band maxima (especially for d–d transitions in the visible region) (Fig. 8). The opposite matching of spectra is shown in Fig. S9.† Though the ECD spectra explore the chirality of the whole molecule, the metal centered chirality, in particular, is reflected in the visible region based on the d–d electron transitions for the open shell metal-complexes.[7–14] Our previous results of variable temperature ^{1}H NMR/ECD/VCD studies suggest the existence of Δ ⇆ Λ equilibrium between the two diastereomers with, in general, diastereomeric excess of Λ-M*RL* or Δ-M*SL* (as major diastereomers) in solutions.[6a,7,9,14] Thus, the comparison of experimental and simulated ECD spectra along with reported literatures infers preferred formation of Λ-Ni*RL*$^{1-2}$ or Δ-Ni*SL*$^{1-2}$ (*i.e.*, diastereomeric excess) over Δ-Ni*RL*$^{1-2}$ or Λ-Ni*SL*$^{1-2}$ in solutions. These results are in parallel with the solid-state X-ray structures of the complexes (Fig. 1) or slightly more stable gas phase optimized structures for Λ-Ni*RL*$^{1-2}$ or Δ-Ni*SL*$^{1-2}$ (Fig. S6†). The overall results thus conclude the integrity of diastereoselection phenomenon and preservation of Δ- or Λ-chirality induction at-nickel upon coordination of *S*- or *R*-HL$^{1-3}$ ligands in solid and solution (or gas phase optimized structures). Similar results of preservation of chirality induction at-metal were reported for the homoleptic Zn(*R* or *S*)L$^{1-3}$ complexes[14] in solid and solution. On the contrary, the homoleptic Cu(*R* or *S*)L$^{1-3}$ complexes[12] showed inversion of chirality induction at-metal from Λ-Cu*RL*$^{1-3}$ or Δ-Cu*SL*$^{1-3}$ in solid to Δ-Cu*RL*$^{1-3}$ or Λ-Cu*SL*$^{1-3}$ in solution.

It was attempted to assign the different electronic transitions based on orbital and population analyses of excited-state properties for Λ-Ni*RL*^{1}.[13,15] Some selected and simplified assignments on simulated spectrum for Λ-NiL^1 are listed in Table 5, which are in good agreement with experimental data. A combined band comprising MM, ML/LM and LL transitions is found at 409 nm with an oscillator strength of 0.0503 and a molecular orbital (MO) contribution of 60% for the HOMO−1 to LUMO transitions. The energy gap between HOMO−1 and LUMO (Fig. 9) is considerably high (ΔEg = 17.96 kcal mol^{-1}), resulting in relatively low MO contributions.

Paramagnetism

^{1}H NMR spectra for Ni*RL*^{1} and Ni*RL*^{2} in dmso-d$_6$ show several broad peaks associated with the co-ordinated Schiff bases to the nickel(II) ion (Fig. S10†). The spectra exhibit shifting and peak broadening effects, corresponding to the paramagnetic nature of the high-spin nickel(II)-complexes in the pseudotetrahedral geometry.[13,15,23]

Powder XRD analysis

Powder XRD patterns (Fig. S11†) for all three pairs of Ni(II)-complexes (Ni*RL*$^{1-3}$/Ni*SL*$^{1-3}$), measured over the 2θ range of 5–50° at ambient temperature, show consistent similarities along the series. Comparison of experimental and simulated PXRD patterns (from single-crystal X-ray structures) reveals a

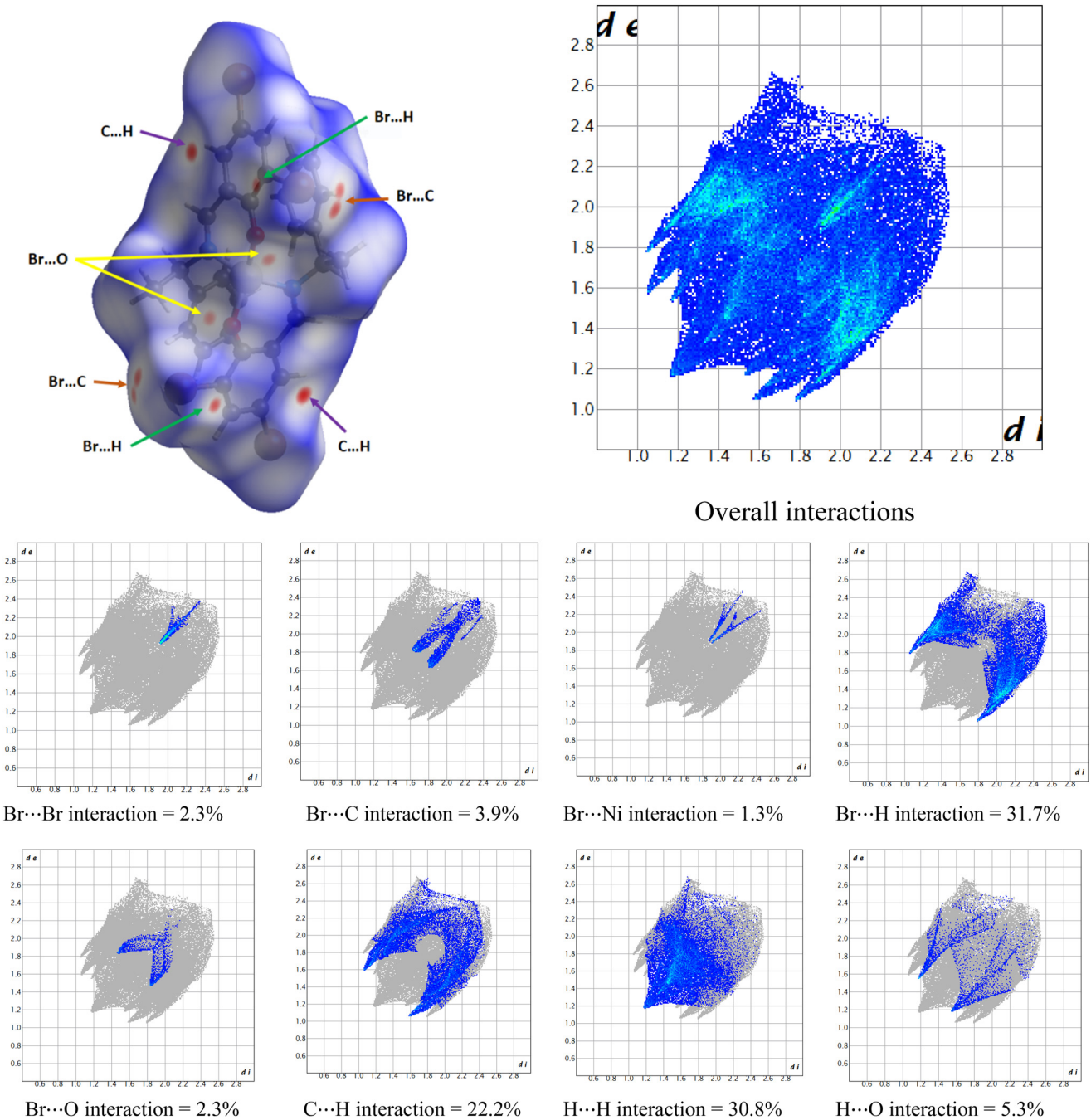

Fig. 4 Hirshfeld surfaces mapped with d_{norm} properties and fingerprint plot for Λ-Ni*R*L^2. Red spots represent the closest contacts and blue the most distant contacts. ESP (electrostatic potential) plotted on Hirshfeld surfaces mapped from −0.875 au (red) to 1.1415 au (blue).

fair matching, confirming the phase purity of bulk crystal samples of the complexes.

Conclusions

The pseudotetrahedral C_2-symmetrical bis[(*S* or *R*)-*N*-1-(phenyl) ethyl-(2,4-X^1,X^2-salicylaldiminato-κ^{2}N,O)]-Δ/Λ-nickel(II), Δ/Λ-Ni*S*L$^{1-3}$ or Λ/Δ-Ni*R*L$^{1-3}$ exhibit Δ- or Λ-chirality induction at-metal upon co-ordination of *S*- or *R*-HL$^{1-3}$ ligands. The X-ray molecular structures proved the formation of Δ-Ni*S*L$^{1-3}$ or Λ-Ni*R*L$^{1-3}$ configured diastereomers in the solid state. This is further supported by slightly more stable gas-phase optimized structures for Δ-Ni*S*L$^{1-2}$ or Λ-Ni*R*L$^{1-2}$. Electronic circular dichroism (ECD) spectra showed the mirror-image relationships, confirming the enantiopurity or enantiomeric excess of Ni*S*L$^{1-3}$ or Ni*R*L$^{1-3}$ in solutions. Combined analyses of experimental and simulated ECD spectra suggested diastereomeric excess of Δ-Ni*S*L$^{1-3}$ or Λ-Ni*R*L$^{1-3}$ in solutions, resulting from diastereoselection and Δ- or Λ-chirality induction at-metal. The overall results thus conclude the preservation of Δ- or Λ-chirality

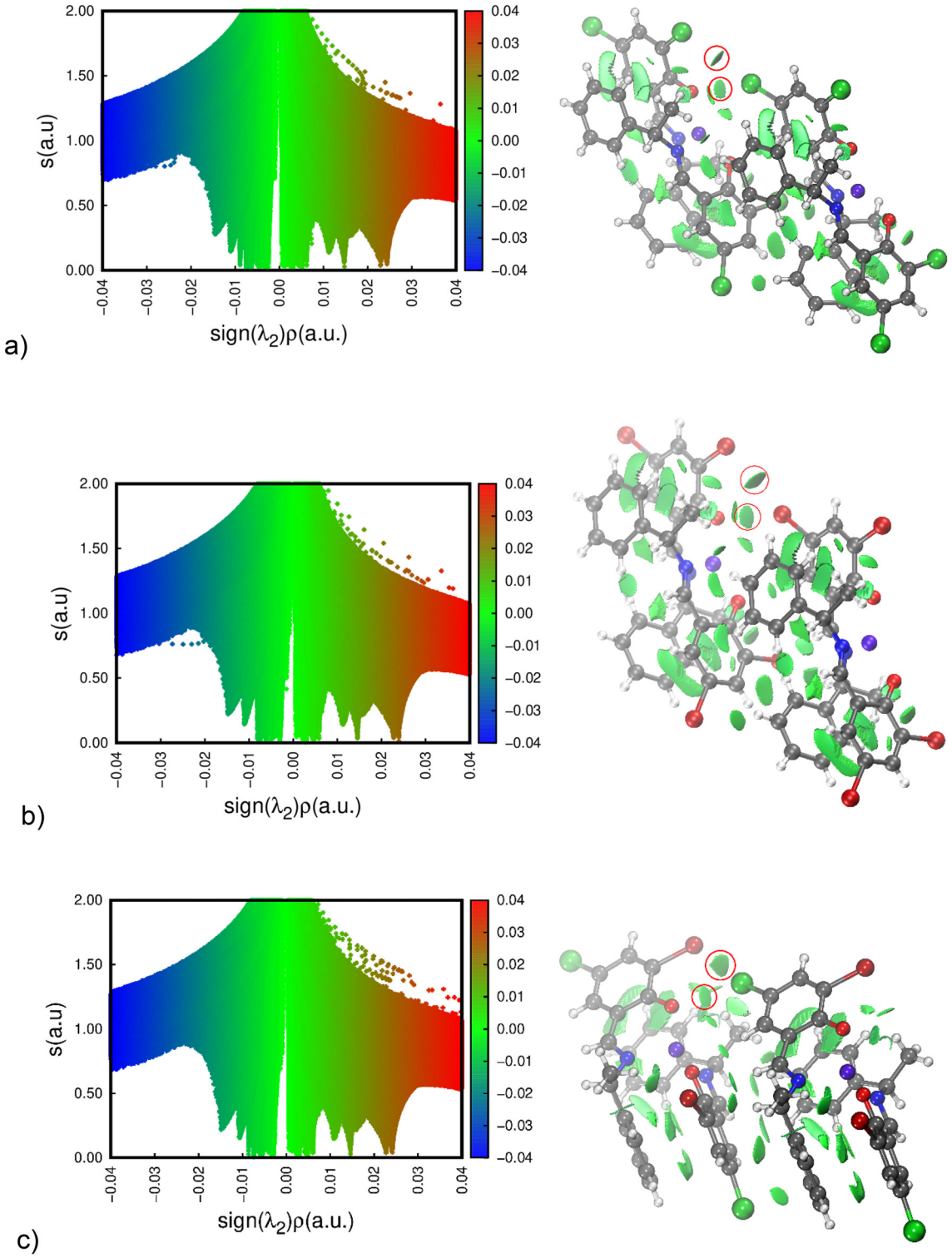

Fig. 5 NCI plots and concomitant interactions at *ca.* $-0.01 \leq \mathrm{sign}(\lambda_2)\rho \leq 0$ between molecules in (a) Δ-Ni*SL*[1], (b) Δ-Ni*SL*[2] and (c) Λ-Ni*RL*[3]. The gradient isosurfaces for the Cl/Br···Cl/Br and Cl/Br···O interactions are highlighted with red circles.

induction at-nickel in solid and solution (or gas-phase optimized structures), alike the homoleptic Zn-complexes[14] and opposite to the homoleptic Cu-complexes (inversion of chirality induction),[12] demonstrating that the metal ion selection plays a key role in phase-dependent diastereoselective phenomenon.

Experimental

Chemicals and instrumentation

$Ni(NO_3)_2{\cdot}6H_2O$ and triethylamine were used as received from the Sigma-Aldrich. The FT-IR spectrum was recorded using a

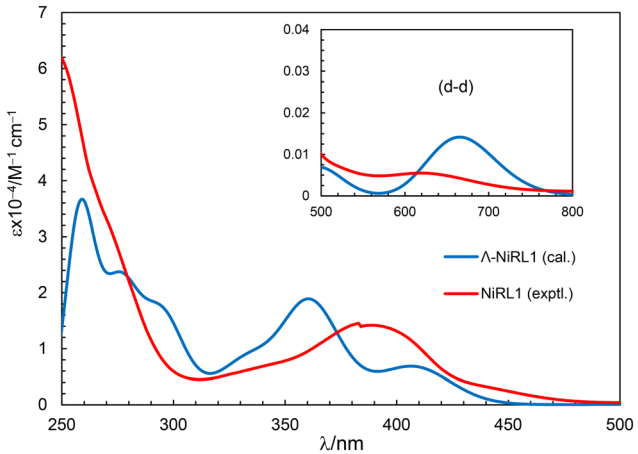

Fig. 6 Experimental and simulated UV-vis spectra for Ni*RL*[1] (2.0 × 10^{-2} mM) in methanol/chloroform (50%, v/v) at 20 °C. Simulated spectrum was calculated at b3lyp/6-31G(d) for Λ-Ni*RL*[1] with PCM in chloroform. Gaussian band shape with an exponential half-width σ = 0.16 eV.

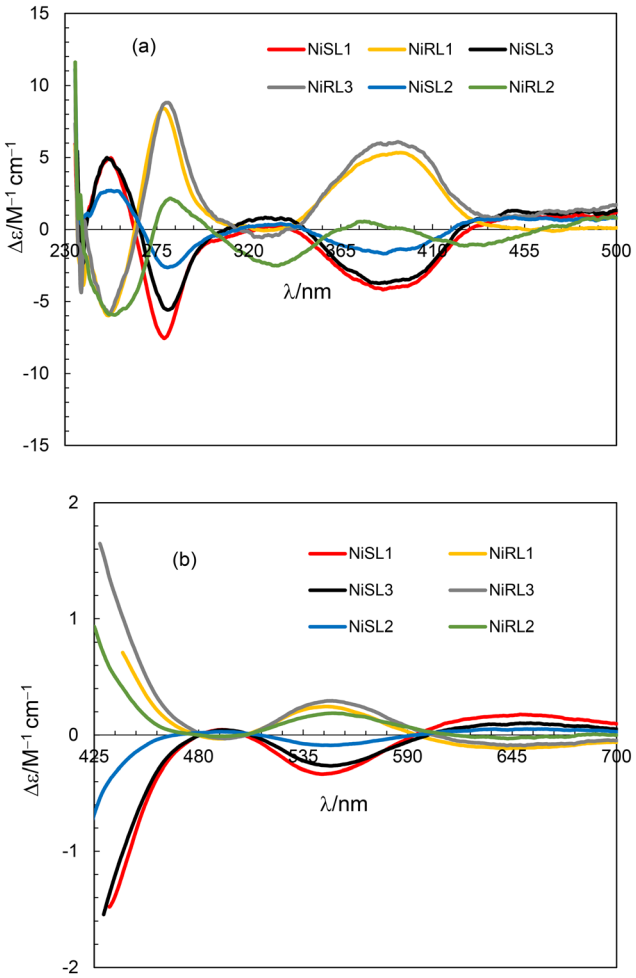

Fig. 7 ECD spectra for the enantiomeric pairs of Ni*RL*[1–3] and Ni*SL*[1–3]: (a) *ca.* 2.0 × 10^{-2} mM at 500–230 nm and (b) *ca.* 1.0 mM at 700–425 nm in methanol/chloroform (50%, v/v) at 20 °C.

JASCO FT/IR-6300 spectrometer (4000–400 cm^{-1}) in KBr pellets. ^{1}H NMR spectra were recorded using a Bruker Avance III 400 spectrometer in dmso-d_6 at 20 °C. The elemental analysis was performed using Leco, CHNS-932 and Perkin-Elmer 7300 DV elemental analyzers. UV-visible spectra were recorded using a Shimadzu UV 1800 spectrophotometer in methanol/chloroform (50%, v/v) at 20 °C. ECD spectra were recorded using a JASCO spectropolarimeter (J 810) in methanol/chloroform (50%, v/v) at 20 °C. Powder XRD patterns for all three pairs of complexes were acquired using a Bruker D2 Phaser powder diffractometer over a 2θ range of 5–50° on a flat silicon, low-background sample holder at 30 kV, 10 mA with Cu-Kα radiation (λ = 1.5418 Å) for 30 min at ambient temperature. The most intense reflection in each diffractogram has been normalized to 1 and matched with the simulated PXRD patterns from single crystal X-ray structure, using the MERCURY 2020.3.0 software.[24] The synthesis of the enantiopure Schiff base ligands, (*R* or *S*)-*N*-1-(phenyl)ethyl-2,4-X^1,X^2-salicylaldimine {(*R* or *S*)-$HL^{1–3}$: X^1, X^2 = Cl, Cl; Br, Br; Cl, Br}, was described in our previous study.[12]

Preparation of the complexes

A solution of triethylamine (7 mmol) in methanol (5 ml) was added to a methanolic solution (10 ml) of appropriate enantiopure Schiff base ligands. The mixture was stirred for 10 min, and then a solution of $Ni(NO_3)_2·6H_2O$ in methanol (10 ml) was added. The resulting solution was refluxed for *ca.* 4 h. Upon addition of salts, immediate precipitation occurs for all complexes except for Ni*RL*[1] and Ni*SL*[1]. The green powder was isolated from the solution and purified by washing with cold methanol. Suitable green crystals for X-ray crystallography were obtained from the concentrated chloroform solution of Ni*RL*[2], Ni*SL*[2], Ni*SL*[3] and Ni*RL*[3], respectively. For Ni*RL*[1] and Ni*SL*[1], the green solution in methanol was slowly evaporated at room temperature to isolate X-ray quality green crystals. The yields for all synthesized complexes are more than 85%.

Ni*RL*[1]: – IR (KBr, cm^{-1}): $\tilde{\nu}$ = 3056, 3033, 2973, 2935w (H–Ar), 1600vs (C═N) and 1577s (C═C). – MS (EI): *m*/*z* (%) = 644 (5) [M = $Ni(L^1)_2]^+$, 351 (30) [$Ni(L^1)$ + H]$^+$, 292 (24) [HL^1–H]$^+$ and 105 (100) [$C_6H_5(CHNH)]^+$ {HL^1 = (*R*)-*N*-1-(phenyl)ethyl-2,4-Cl,Cl-salicylaldimine = $C_{15}H_{12}Cl_2NOH$}. Anal. calc. For $C_{30}H_{24}Cl_4NiN_2O_2$: C, 55.86; H, 3.75; N, 4.34%. Found: C, 55.83; H, 3.72; N, 3.35%.

Ni*SL*[1]: – IR (KBr, cm^{-1}): $\tilde{\nu}$ = 3064, 3032, 2978, 2939w (H–Ar), 1600vs (C═N) and 1575sh (C═C). – MS (EI): *m*/*z* (%) = 644 (7) [M = $Ni(L^1)_2]^+$, 351 (32) [$Ni(L^1)$ + H]$^+$, 292 (28) [HL^1–H]$^+$ and 105 (100) [$C_6H_5(CHNH)]^+$ {HL^1 = (*S*)-*N*-1-(phenyl) ethyl-2,4-Cl,Cl-salicylaldimine = $C_{15}H_{12}Cl_2NOH$}. Anal. calc. For $C_{30}H_{24}Cl_4NiN_2O_2$: C, 55.86; H, 3.75; N, 4.34%. Found: C, 55.88; H, 3.75; N, 3.33%.

Ni*RL*[2]: – IR (KBr, cm^{-1}): $\tilde{\nu}$ = 3056, 3033, 2973, 2935w (H–Ar), 1600vs (C═N) and 1577s (C═C). – MS (EI): *m*/*z* (%) = 823 (1) [M + H = $Ni(L^2)_2$ + H]$^+$, 441 (10) [$Ni(L^2)$ + H]$^+$, 383 (8) [HL^2]$^+$, 279 (12) [$C_6H_2(Br_2)(CHNH)(OH)]^+$ and 105 (100) [$C_6H_5(CHNH)]^+$ {HL^2 = (*R*)-*N*-1-(phenyl)ethyl-2,4-Br,Br-salicylaldimine = $C_{15}H_{12}Br_2NOH$}. Anal. calc. For $C_{30}H_{24}Br_4NiN_2O_2$: C, 43.79; H, 2.94; N, 3.40%. Found: C, 43.81; H, 2.93; N, 3.44%.

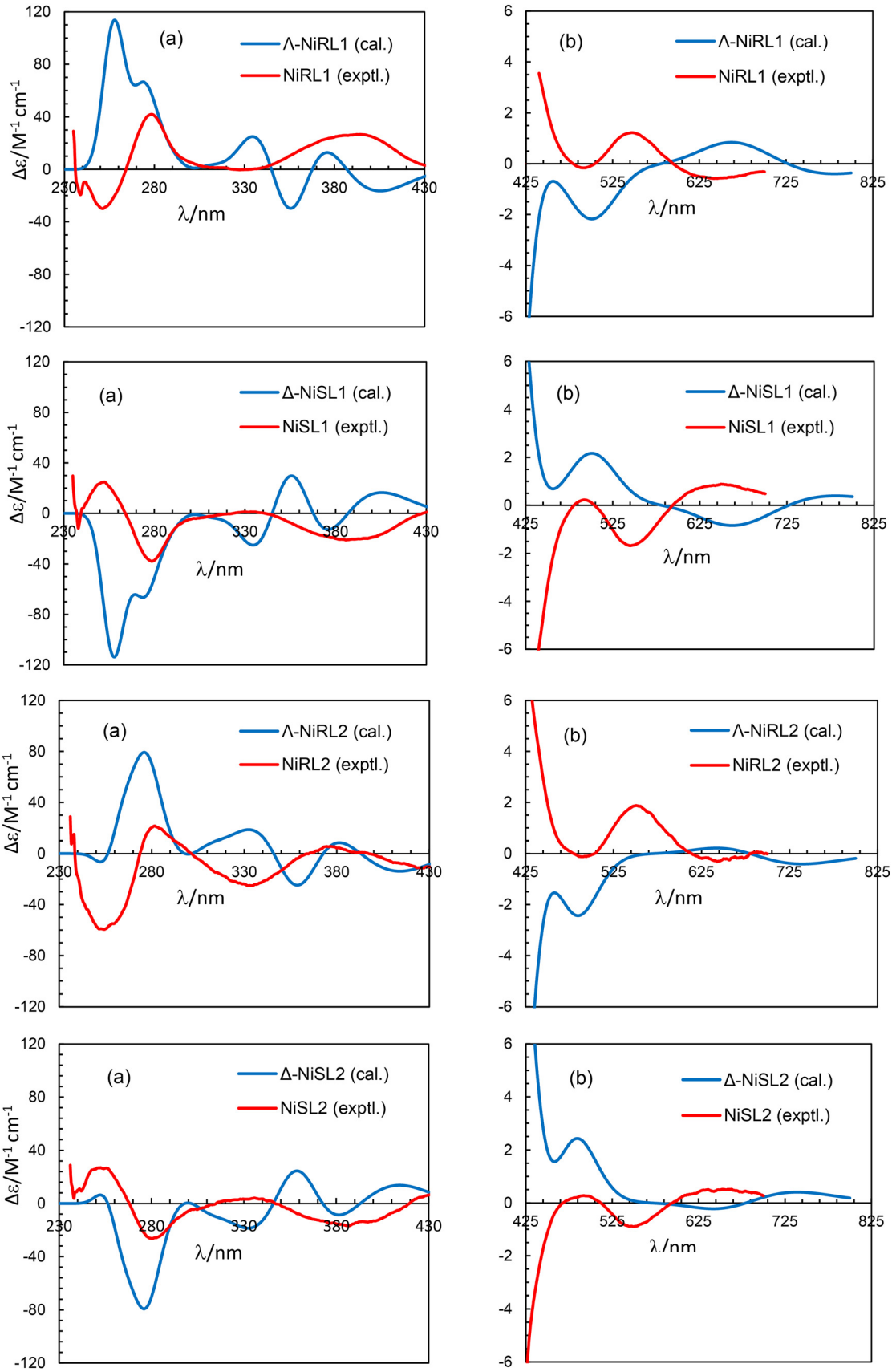

Fig. 8 Comparisons of experimental and simulated ECD spectra (fair matching). Experimental spectra: (a) *ca.* 2.0 × 10^{-2} mM at 430–230 nm and (b) *ca.* 1.0 mM at 825–425 nm in methanol/chloroform (50%, v/v) at 20 °C ($\Delta\varepsilon_{exptl.}$ values are multiplied by 5). Simulated spectra were calculated at b3lyp/6-31G(d) with PCM in chloroform. Gaussian band shape with exponential half-width σ = 0.16 eV.

Table 5 Some selected and simplified assignments on electronic absorption spectrum for Λ-Ni*R*L[1], calculated at b3lyp/6-31G(d)[a]

λ^b/nm	Oscill. strength (f)	Transitions[c] (%)	Assignments[d]
666 (630)	0.0014	H-6 → L + 3 (21), H-4 → L + 3 (16)	LM
409 (445 sh)	0.0503	H-1 → L (60), H-1 → L + 2 (9)	MM, ML/LM, LL
363 (392)	0.1015	H → L + 1 (59)	LM, LL
296	0.1064	H-5 → L (25), H-2 → L + 2 (15)	ML/LM, LL
274 (270 sh)	0.1198	H-5 → L + 2 (19), H-2 → L + 2 (22)	ML, LL
257 (245)	0.2093	H-16 → L (22), H-14 → L (19)	LM, LL

[a] Assignments are made for β-spin MOs consideration. [b] Experimental values are in parentheses. [c] H/L = HOMO/LUMO. [d] MM = d–d, ML/LM = metal–ligand/ligand–metal and LL = intra-ligand transitions.

Ni*S*L[2]: – IR (KBr, cm^{-1}): $\tilde{\nu}$ = 3055, 3033, 2973, 2935w (H–Ar), 1599vs (C═N) and 1576s (C═C). – MS (EI): *m*/*z* (%) = 383 (10) [HL[2]]$^+$, 279 (20) [$C_6H_2(Br_2)$(CHNH)(OH)]$^+$ and 105 (100) [C_6H_5(CHNH)]$^+$ {HL[2] = (*S*)-*N*-1-(phenyl)ethyl-2,4-Br,Br-salicylaldimine = $C_{15}H_{12}Br_2NOH$}. Anal. calc. For $C_{30}H_{24}Br_4NiN_2O_2$: C, 43.79; H, 2.94; N, 3.40%. Found: C, 43.81; H, 2.91; N, 3.43%.

Ni*R*L[3]: – IR (KBr, cm^{-1}): $\tilde{\nu}$ = 3058, 3031, 2975, 2937w (H–Ar), 1601vs (C═N) and 1575sh (C═C). – MS (EI): *m*/*z* (%) = 734 (2) [M = Ni(L[3])$_2$]$^+$, 397 (22) [Ni(L[3]) + H]$^+$, 338 (11) [HL[3]–H]$^+$ and 105 (100) [C_6H_5(CHNH)]$^+$ {HL[3] = (*R*)-*N*-1-(phenyl) ethyl-2,4-Cl,Br-salicylaldimine = $C_{15}H_{12}ClBrNOH$}. Anal. calc. For $C_{30}H_{24}Cl_2Br_2NiN_2O_2$: C, 49.09; H, 3.30; N, 3.82%. Found: C, 49.11; H, 3.27; N, 3.83%.

Ni*S*L[3]: – IR (KBr, cm^{-1}): $\tilde{\nu}$ = 3058, 3032, 2975, 2937w (H–Ar), 1601vs (C═N) and 1576sh (C═C). – MS (EI): *m*/*z* (%) = 734 (3) [M = Ni(L[3])$_2$]$^+$, 397 (20) [Ni(L[3]) + H]$^+$, 338 (15) [HL[3]–H]$^+$ and 105 (100) [C_6H_5(CHNH)]$^+$ {HL[3] = (*S*)-*N*-1-(phenyl) ethyl-2,4-Cl,Br-salicylaldimine = $C_{15}H_{12}ClBrNOH$}. Anal. calc. For $C_{30}H_{24}Cl_2Br_2NiN_2O_2$: C, 49.09; H, 3.30; N, 3.82%. Found: C, 49.10; H, 3.29; N, 3.81%.

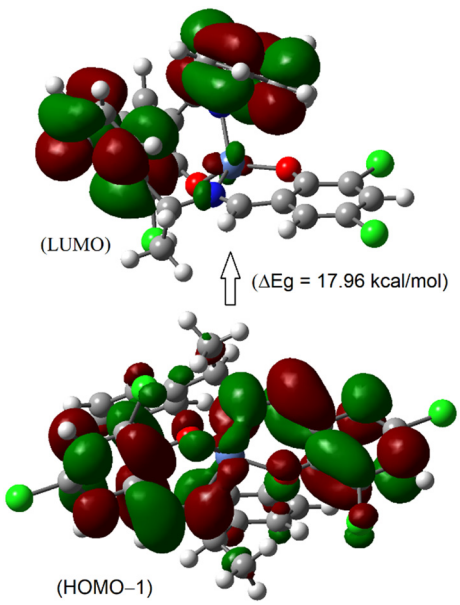

Fig. 9 Frontier HOMO–1 and LUMO for Λ-Ni*R*L[1], calculated at b3lyp/6-31G(d) for β-spin MO consideration.

X-ray crystal crystallography

Single-crystal X-ray diffraction data for all Ni(II) complexes except Δ-Ni*S*L[2] were collected at 160(1) K using a Rigaku OD XtaLAB Synergy, Dualflex, Pilatus 200 K diffractometer with a single-wavelength X-ray source (MoK$_\alpha$ radiation: λ = 0.71073 Å) from a micro-focus sealed X-ray tube and an Oxford liquid-nitrogen Cryostream cooler. Single-crystal X-ray diffraction data for Δ-Ni*S*L[2] was collected at 160(1) K using a Rigaku OD SuperNova/Atlas area-detector diffractometer with CuK$_\alpha$ radiation (λ = 1.54184 Å) from a micro-focus X-ray source and an Oxford Instruments Cryojet XL cooler. The selected suitable single crystal was mounted using polybutene oil on a flexible loop fixed on a goniometer head and immediately transferred to the diffractometer. Pre-experiment, data collection, data reduction and analytical absorption correction[25] were performed with the program suite CrysAlisPro.[26] Using Olex2,[27] structure was solved with the SHELXT[28] small-molecule structure solution program and refined using the SHELXL2018/3 program package[29] by full-matrix least-squares minimization on F^2. Hydrogen atoms were placed in calculated positions by means of the "riding" model. PLATON[30] was used to check results of X-ray analyses. More details concerning the crystallographic data and structures refinements are given in Table S1.†

Computational methods

A thorough computational procedure was employed using Gaussian 09.[31] The initial gas-phase geometries for Λ-Ni*R*L[1–3]/Λ-Ni*S*L[1–3] were generated from their corresponding single-crystal X-ray structures. The geometries with opposite configuration at-metal (*i.e.*, for Λ-Ni*R*L[1–3]/Λ-Ni*S*L[1–3]) were designed by mirror inversion of the structures following manual inversion of the chiral carbon center.[3,4,8–12] The structures were then optimized by DFT at b3lyp/6-31G(d), respectively (Fig. S7†).[13,15] To gain insights into the electronic transitions and chiroptical properties, excited state properties by TD-DFT were calculated at b3lyp/6-31G(d). The PCM (polarization continuum model) was incorporated using chloroform as the solvent and 72 excited states (roots) were considered for calculations (Table S2†). The simulated spectra (UV-vis and ECD) were illustrated using the program SpecDis[32] with Gaussian band shape with exponential half-width σ = 0.16 eV. Finally, assignments on the electronic transitions on simulated

spectra and molecular orbitals (MOs) calculations were made for Λ-Ni*R*L[1] at the same level of theory.

The NCI plots were generated for systems Δ-Ni*S*L[1], Δ-Ni*S*L[2] and Λ-Ni*R*L[3] with NCIPLOT4.[33] Molecular densities were computed with Gaussian 16 (ref. 31) performed at a b3lyp/def2-tzvp level of theory and Grimme-D3 dispersion correction.[34] NCI surfaces were visualized with VMD.[35]

Conflicts of interest

There are no conflicts to declare.

Acknowledgements

We acknowledge the financial support from the Alexander von Humboldt Foundation (AvH), Bonn, Germany under the project Research Group Linkage Program and the Research Council of the University of Isfahan, Iran. We thank Professor ABP Lever, Department of Chemistry, York University, Toronto and the computecanada.ca (**https://ccdb.computecanada.ca/**) Ontario, Canada, for using computational resources. Computational infrastructure and support were provided by the Centre for Information and Media Technology at Heinrich Heine University Düsseldorf, Germany.

Notes and references

1 (*a*) H. Amouri and M. Gruselle, *Chirality in Transition Metal Chemistry: Molecules, supramolecular assemblies and materials*, John Wiley & Sons, Chichester, 2008, p. 40; (*b*) A. von Zelewsky, *Stereochemistry of Coordination Compounds*, John Wiley & Sons, Chichester, 1996, p. 69; (*c*) E. C. Constable, *Chem. Soc. Rev.*, 2013, **42**, 1637; (*d*) K. A. Jensen, *Inorg. Chem.*, 1970, **9**, 1; (*e*) U. Knof and A. von Zelewsky, *Angew. Chem., Int. Ed.*, 1999, **38**, 302; (*f*) O. Mamula, A. von Zelewsky, T. Bark, H. Stoeckli-Evans, A. Neels and G. Bernardinelli, *Chem. – Eur. J.*, 2000, **6**, 3575.

2 (*a*) C. Evans and D. Luneau, *J. Chem. Soc., Dalton Trans.*, 2002, 83; (*b*) R. E. Ernst, M. J. O'Connor and R. H. Holm, *J. Am. Chem. Soc.*, 1967, **89**, 6104; (*c*) G. Brewer, C. Brewer, R. J. Butcher, G. T. Robichaux and C. Viragh, *Inorg. Chim. Acta*, 2014, **410**, 171; (*d*) S. E. Howson and P. Scott, *Dalton Trans.*, 2011, **40**, 4332; (*e*) J. M. Becker, J. Barker, G. J. Clarkson, R. van Gorkum, G. K. Johal, R. I. Walton and P. Scott, *Dalton Trans.*, 2010, **39**, 2309.

3 (*a*) E. C. Constable, G. Zhang, C. E. Housecroft, M. Neuburger and J. A. Zampese, *Chem. Commun.*, 2010, 3077; (*b*) F. Wang, H. Zhang, L. Li, H.-Q. Hao, X.-Y. Wang and J.-G. Chen, *Tetrahedron: Asymmetry*, 2006, **17**, 2059; (*c*) T. Ohno, S. Chorazy, K. Imoto and S. Ohkoshi, *Cryst. Growth Des.*, 2016, **16**, 4119; (*d*) H. Song, M. Postings, P. Scott and N. J. Rogers, *Chem. Sci.*, 2021, **12**, 1620.

4 (*a*) H. Sakiyama, H. Okawa, N. Matsumoto and S. Kida, *Bull. Chem. Soc. Jpn.*, 1991, **64**, 2644; (*b*) H. Sakiyama, H. Okawa, N. Matsumoto and S. Kida, *J. Chem. Soc., Dalton Trans.*, 1990, 2935; (*c*) Z. Dezhahang, M. R. Poopari, J. Cheramy and Y. J. Xu, *Inorg. Chem.*, 2015, **54**, 4539.

5 (*a*) H. Ōkawa, M. Nakamura and S. Kida, *Inorg. Chim. Acta*, 1986, **120**, 185; (*b*) T. Akitsu and Y. Einaga, *Polyhedron*, 2005, **24**, 2933; (*c*) T. Akitsu and Y. Einaga, *Polyhedron*, 2005, **24**, 1869; (*d*) T. Akitsu and Y. Einaga, *Acta Crystallogr., Sect. C: Cryst. Struct. Commun.*, 2004, **60**, m640; (*e*) T. Akitsu, *Polyhedron*, 2007, **26**, 2527.

6 (*a*) A.-C. Chamayou, S. Lüdeke, V. Brecht, T. B. Freedman, L. A. Nafie and C. Janiak, *Inorg. Chem.*, 2011, **50**, 11363; (*b*) A.-C. Chamayou, G. Makhloufi, L. A. Nafie, C. Janiak and S. Lüdeke, *Inorg. Chem.*, 2015, **54**, 2193.

7 G. Pescitelli, S. Lüdeke, A.-C. Chamayou, M. Marolt, V. Justus, M. Górecki, L. Arrico, L. Di Bari, M. A. Islam, I. Gruber, M. Enamullah and C. Janiak, *Inorg. Chem.*, 2018, **57**, 13397.

8 M. Enamullah, A. K. M. Royhan Uddin, G. Pescitelli, R. Berardozzi, G. Makhloufi, V. Vasylyeva, A.-C. Chamayou and C. Janiak, *Dalton Trans.*, 2014, **43**, 3313.

9 M. Enamullah, G. Makhloufi, R. Ahmed, B. Alif Joy, M. A. Islam, D. Padula, H. Hunter, G. Pescitelli and C. Janiak, *Inorg. Chem.*, 2016, **55**, 6449.

10 M. Górecki, M. Enamullah, M. A. Islam, M. K. Islam, S.-P. Höfert, D. Woschko, C. Janiak and G. Pescitelli, *Inorg. Chem.*, 2021, **60**, 14116.

11 M. Enamullah, M. A. Hossain, M. K. Islam, D. Woschko and C. Janiak, *Dalton Trans.*, 2021, **50**, 9236.

12 N. Kordestani, H. A. Rudbari, G. Bruno, S. Rosario, J. D. Braun, D. E. Herbert, O. Blacque, I. Correia, M. A. Zaman, M. M. Bindu, C. Janiak and M. Enamullah, *Dalton Trans.*, 2020, **49**, 8247.

13 M. Enamullah, M. A. Quddus, M. R. Hasan, G. Pescitelli, R. Berardozzi, G. Makhloufi, V. Vasylyeva and C. Janiak, *Dalton Trans.*, 2016, **45**, 667.

14 H. A. Rudbari, A. Saadati, M. Aryaeifar, O. Blacque, I. Correia, M. K. Islam, D. Woschko, C. Janiak and M. Enamullah, *Dalton Trans.*, 2022, **51**, 2385.

15 M. Enamullah, M. A. Quddus, M. R. Hasan, G. Pescitelli, R. Berardozzi, G. J. Reiß and C. Janiak, *Eur. J. Inorg. Chem.*, 2015, 2758.

16 (*a*) M. Enamullah, A. K. M. Royhan Uddin, A.-C. Chamayou and C. Janiak, *Z. Naturforsch., B: J. Chem. Sci.*, 2007, **62**, 807; (*b*) M. Enamullah, A. K. M. Royhan Uddin, G. Hogarth and C. Janiak, *Inorg. Chim. Acta*, 2012, **387**, 173.

17 (*a*) Y. Shibuya, K. Nabari, M. Kondo, S. Yasue, K. Maeda, F. Uchida and H. Kawaguchi, *Chem. Lett.*, 2008, **37**, 78; (*b*) L. Yang, D. R. Powell and R. P. Houser, *Dalton Trans.*, 2007, 955.

18 (*a*) H. D. Flack, M. Sadki, A. L. Thompson and D. J. Watkin, *Acta Crystallogr., Sect. A: Found. Crystallogr.*, 2011, **67**, 21; (*b*) H. D. Flack and G. Bernardinelli, *Chirality*, 2008, **20**, 681.

19 (*a*) H. D. Flack and G. Bernardinelli, *Acta Crystallogr., Sect. A: Found. Crystallogr.*, 1999, **55**, 908; (*b*) H. Flack, *Acta Crystallogr., Sect. A: Found. Crystallogr.*, 1983, **39**, 876.

20 A. V. Bondi, *J. Phys. Chem.*, 1964, **68**, 441.

21 M. J. Turner, J. J. McKinnon, S. K. Wolff, D. J. Grimwood, P. R. Spackman, D. Jayatilaka and M. A. Spackman, *CrystalExplorer 17*, University of Western Australia, 2017, **https://hirshfeldsurface.net**.

22 (*a*) J. J. McKinnon, M. A. Spackman and A. S. Mitchell, *Acta Crystallogr., Sect. B: Struct. Sci.*, 2004, **60**, 627; (*b*) M. A. Spackman and J. J. McKinnon, *CrystEngComm*, 2002, **4**, 378; (*c*) J. J. McKinnon, D. Jayatilaka and M. A. Spackman, *Chem. Commun.*, 2007, 3814; (*d*) P. R. Spackman, M. J. Turner, J. J. McKinnon, S. K. Wolff, D. J. Grimwood, D. Jayatilaka and M. A. Spackman, *J. Appl. Crystallogr.*, 2021, **54**, 1006.

23 M. Enamullah and A. K. M. Royhan Uddin, *J. Bangladesh Chem. Soc.*, 2009, **22**, 44.

24 C. F. Macrae, I. Sovago, S. J. Cottrell, P. T. A. Galek, P. McCabe, E. Pidcock, M. Platings, G. P. Shields, J. S. Stevens, M. Towler and P. A. Wood, *J. Appl. Crystallogr.*, 2020, **53**, 226.

25 R. C. Clark and J. S. Reid, *Acta Crystallogr., Sect. A: Found. Crystallogr.*, 1995, **51**, 887.

26 *CrysAlisPro (version 1.171.40.103a)*, Rigaku Oxford Diffraction, 2021.

27 O. V. Dolomanov, L. J. Bourhis, R. J. Gildea, J. A. K. Howard and H. Puschmann, *J. Appl. Crystallogr.*, 2009, **42**, 339.

28 G. M. Sheldrick, *Acta Crystallogr., Sect. A: Found. Adv.*, 2015, **71**, 3.

29 G. M. Sheldrick, *Acta Crystallogr., Sect. C: Struct. Chem.*, 2015, **71**, 3.

30 A. L. Spek, *Acta Crystallogr., Sect. D: Biol. Crystallogr.*, 2009, **65**, 148.

31 M. J. Frisch, G. W. Trucks, H. B. Schlegel, G. E. Scuseria, M. A. Robb, J. R. Cheeseman, G. Scalmani, V. Barone, B. Mennucci, G. A. Petersson, H. Nakatsuji, M. Caricato, X. Li, H. P. Hratchian, A. F. Izmaylov, J. Bloino, G. Zheng, J. L. Sonnenberg, M. Hada, M. Ehara, K. Toyota, R. Fukuda, J. Hasegawa, M. Ishida, T. Nakajima, Y. Honda, O. Kitao, H. Nakai, T. Vreven, J. A. Montgomery Jr. , J. E. Peralta, F. Ogliaro, M. Bearpark, J. J. Heyd, E. Brothers, K. N. Kudin, V. N. Staroverov, R. Kobayashi, J. Normand, K. Raghavachari, A. Rendell, J. C. Burant, S. S. Iyengar, J. Tomasi, M. Cossi, N. Rega, J. M. Millam, M. Klene, J. E. Knox, J. B. Cross, V. Bakken, C. Adamo, J. Jaramillo, R. Gomperts, R. E. Stratmann, O. Yazyev, A. J. Austin, R. Cammi, C. Pomelli, J. W. Ochterski, R. L. Martin, K. Morokuma, V. G. Zakrzewski, G. A. Voth, P. Salvador, J. J. Dannenberg, S. Dapprich, A. D. Daniels, Ö. Farkas, J. B. Foresman, J. V. Ortiz, J. Cioslowski and D. J. Fox, *Gaussian 09, Revision D.01*, Gaussian, Inc., Wallingford CT, 2009.

32 (*a*) T. Bruhn, A. Schaumlöffel, Y. Hemberger and G. Bringmann, *Chirality*, 2013, **25**, 243; (*b*) T. Bruhn, A. Schaumlöffel, Y. Hemberger and G. Pescitelli, *SpecDis version 1.71*, Berlin, Germany, 2017, **https://specdis-software.jimdo.com/**.

33 R. Boto, F. Peccati, R. Laplaza, C. Quan, A. Carbone, J.-P. Piquemal, Y. Maday and J. Contreras-García, *NCIPLOT4: A New Step Towards a Fast Quantification of Noncovalent Interactions*, 2020.

34 S. Grimme, J. Antony, S. Ehrlich and H. Krieg, *J. Chem. Phys.*, 2010, **132**, 154104.

35 W. Humphrey, A. Dalke and K. Schulten, *J. Mol. Graphics*, 1996, **14**, 33.